Available online at www.sciencedirect.com
ScienceDirect
Thermochimica Acta 467 (2008) 11–19
thermochimica acta
www.elsevier.com/locate/tca

Thermal decomposition of synthetic antlerite prepared by microwave-assisted hydrothermal method

Nobuyoshi Koga *, Akira Mako, Takaaki Kimizu, Yuu Tanaka

Chemistry Laboratory, Graduate School of Education, Hiroshima University, 1-1-1 Kagamiyama, Higashi-Hiroshima 739-8524, Japan

Received 6 August 2007; received in revised form 22 October 2007; accepted 26 October 2007
Available online 4 November 2007

Abstract

Copper(II) hydroxide sulfate was synthesized by a microwave-assisted hydrothermal method from a mixed solution of $CuSO_4$ and urea. Needle-like crystals of ca. 20–30 μm in length precipitated by irradiating microwave for 1 min were characterized as $Cu_3(OH)_4SO_4$ corresponding to mineral antlerite. The reaction pathway and kinetics of the thermal decomposition of the synthetic antlerite $Cu_3(OH)_4SO_4$ were investigated by means of thermoanalytical techniques complemented by powder X-ray diffractometry and microscopic observations. The thermal decomposition of $Cu_3(OH)_4SO_4$ proceeded via two separated reaction steps of dehydroxylation and desulfation to produce CuO, where crystalline phases of Cu_2OSO_4 and CuO appeared as the intermediate products. The kinetic characteristics of the respective steps were discussed in comparison with those of the synthetic brochantite $Cu_4(OH)_6SO_4$ reported previously.

Keywords: Microwave-assisted hydrothermal synthesis; Antlerite; Thermal decomposition; Reaction pathway; Kinetics

1. Introduction

Because various basic copper(II) salts are suitable precursors for CuO with various desired properties and appear as a co-precipitate in the precursors for many Cu-containing ceramics, it is expected that detailed investigations on the kinetics and mechanisms of the thermal decomposition of basic copper(II) salts provide valuable information to improve the ceramic processing through thermal decomposition route. Along this line, we have reported the kinetic characteristics of the thermal decompositions of copper(II) hydroxide sulfate [1] and copper(II) hydroxide carbonate [2–4].

As for copper(II) hydroxide sulfate, in addition to brochantite $Cu_4(OH)_6SO_4$ which was subjected previously to the study on the reaction pathway and kinetics of the thermal decomposition processes [1], an alternative copper(II) hydroxide sulfate corresponding to mineral antlerite $Cu_3(OH)_4SO_4$ is known [5–11]. Synthetic antlerite has been prepared by hydrothermal methods from a mixed solution of $CuSO_4$ and urea [5], suspension of CuO or $Cu(OH)_2$ in $CuSO_4$ solution [6,9], or a mixed solution of $CuSO_4$ and NaOH [10,11], where the starting solutions were digested for the hydrothermal treatments at 110–170 °C for several days or weeks. Reaction pathway of the thermal decomposition of synthetic antlerite has been studied by thermoanalytical techniques, IR spectrometry and X-ray diffractometry [5–7,9], indicating that the thermal decomposition proceeds in two separated reaction steps of dehydroxylation and desulfation reactions via mixed intermediate products of Cu_2OSO_4 and CuO. The detailed kinetics and mechanisms of the respective reaction steps of the thermal decomposition have not been clarified as yet.

In the present study, a rapid synthesis of antlerite was examined by applying microwave-assisted hydrothermal method [12] for a mixed solution of $CuSO_4$ and urea. The precipitates obtained were characterized by various techniques in comparison with the previously reported data for synthetic antlerite and also for synthetic brochantite. The reaction pathway and physico-chemical events taking place during the course of the thermal decomposition processes were reinvestigated in order to find some kinetic-related phenomena required to interpret the kinetic results. Kinetic analyses for the respective reaction steps were carried out for the kinetic rate data under linearly increasing temperature. The kinetic characteristics of the respective reaction steps were discussed in

* Corresponding author.
E-mail address: nkoga@hiroshima-u.ac.jp (N. Koga).

0040-6031/$ – see front matter © 2007 Elsevier B.V. All rights reserved.
doi:10.1016/j.tca.2007.10.016

comparison with those for synthetic brochantite reported previously.

2. Experimental

2.1. Sample preparation and characterization

An aqueous solution of 0.1 M $CuSO_4$ was mixed with urea solutions of various concentrations so as the molar ratio of urea/Cu^{2+} to be 0.5–2.0. The mixed solutions of 10 cm^3 were put into a Teflon reactor constructed by 25 cm^3 inner Teflon vessel with a lid and outer polypropylene vessel with a screw cap. Using a domestic microwave oven, microwaves (2.45 GHz, 700 W) were irradiated to the reactor for 1 min. After cooling the reactor to room temperature, the precipitates produced were filtered, washed with water, and dried in a desiccator.

The samples were subjected to chemical analyses for Cu^{2+} and SO_4^{2-} by the iodometry and gravimetry as $BaSO_4$, respectively. Characterization of the samples was also made by TG–DTA (Shimazu TGD-50), FT-IR spectroscopy (Shimadzu FTIR8400S), and powder X-ray diffractometry (Rigaku RINT-2200V). Morphology of the sample particles was observed using a scanning electron microscope (Hitachi S-2460N).

2.2. Tracing of thermal decomposition processes

The sample of ca. 500 mg was heated at various temperatures from 373 to 1073 K for 30 min in an electric furnace in air. The annealed samples were characterized by the measurements of specific surface area using single-point BET method (Micromeritics FlowSorbII-2300), in addition to the above-mentioned techniques. For obtaining the kinetic rate data for the thermal decomposition processes, the sample of 5.0 mg was subjected to the measurements of TG (Shimadzu TGA-50) at various heating rates under flowing N_2 (80 $cm^3\,min^{-1}$). The course of reaction of a selected decomposition step was also traced by the change in the XRD pattern using the above-described XRD instrument by equipping with a programmable heating chamber (Rigaku PTC-20A). By heating the samples at a linear heating rate of 5 $K\,min^{-1}$ under flowing N_2 (100 $cm^3\,min^{-1}$), XRD patterns were measured at various temperatures where the sample temperature was kept constant during the diffraction measurements.

3. Results and discussions

3.1. Sample characterization

Fig. 1 shows a typical SEM image of the sample precipitated in the Teflon reactor by the microwave-assisted heating for 1 min. Irrespective of molar ratios of urea/Cu^{2+} of the mother solutions, the sample particles were the aggregate of needle-like crystallites (ca. 20–30 μm in length) radiating from a crystal of flat prism to all directions, where flat prism crystals seems to act as seed of the growth of the needle-like crystallites. The contents of Cu^{2+} and SO_4^{2-} in the samples precipitated from the mother solutions with different molar ratios of urea/Cu^{2+} were

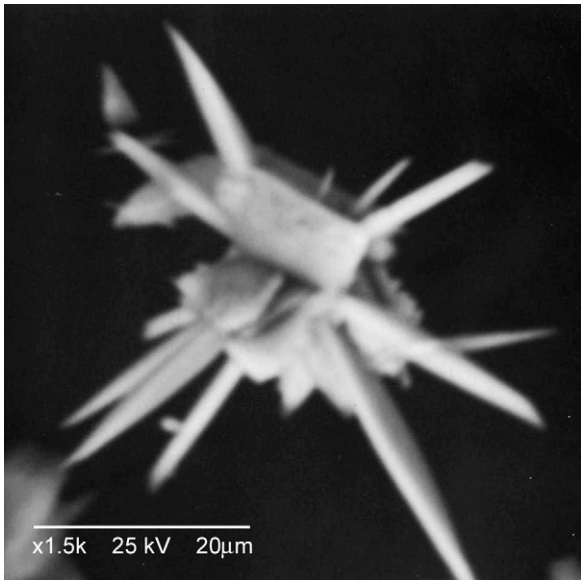

Fig. 1. A typical SEM image of the sample precipitated by the microwave-assisted hydrothermal method for digesting a mixed solution of $CuSO_4$ and urea to microwave irradiation for 1 min.

listed in Table 1. All the samples indicated practically the same contents of Cu^{2+} and SO_4^{2-}, which are closely corresponding to the values calculated for antlerite $Cu_3(OH)_4SO_4$ rather than brochantite $Cu_4(OH)_6SO_4$.

Results of the further characterization of the sample and its thermal decomposition processes are reported by selecting the sample prepared from the mother solution with molar ratio of urea/Cu^{2+} = 1.0, because any notable differences cannot be found among the samples. Fig. 2 shows typical XRD patterns of the present sample, together with that for synthetic brochantite $Cu_4(OH)_6SO_4$ prepared by titrating a 0.1 M $CuSO_4$ solution with a 0.1 M NaOH solution until pH 10 [13]. The present sample indicated completely different XRD pattern from that of synthetic brochantite and all the major diffraction peaks corresponded to that of synthetic antlerite $Cu_3(OH)_4SO_4$ [8,11,14]. Fig. 3 compares typical IR spectra for the present sample and synthetic brochantite $Cu_4(OH)_6SO_4$. The profile of the IR spectrum for the present sample is in good agreement with the IR spectra reported for the synthetic antlerite $Cu_3(OH)_4SO_4$ [5,7]. Making a comparison between the IR spectra for the present sample and $Cu_4(OH)_6SO_4$, contrasting features can be seen for the O–H stretching vibration in 3600–3200 cm^{-1}. It

Table 1
Contents of Cu^{2+} and SO_4^{2-} in the samples precipitated hydrothermally from the mother solutions of various molar ratios of urea/$CuSO_4$

Molar ratio urea/$CuSO_4$	Cu^{2+} (%)	SO_4^{2-} (%)
0.5	53.3 ± 0.4	26.9 ± 0.5
1.0	53.1 ± 0.2	26.3 ± 0.6
1.5	53.0 ± 0.2	26.7 ± 0.4
2.0	53.6 ± 0.1	26.0 ± 0.7
$Cu_4(OH)_6SO_4$	56.2[a]	21.2[a]
$Cu_3(OH)_4SO_4$	53.8[a]	27.1[a]

[a] Calculated.

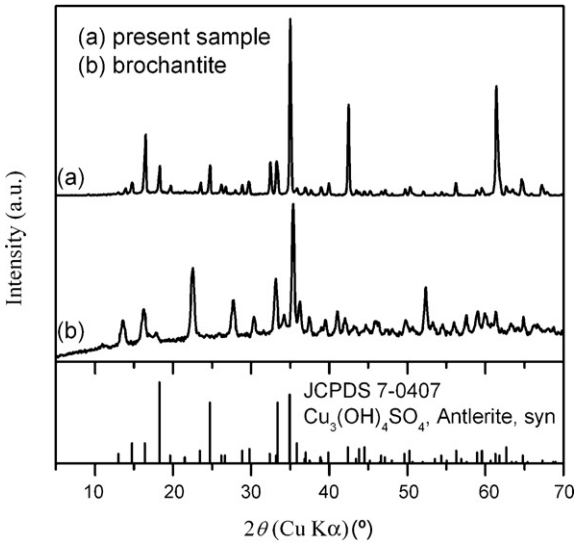

Fig. 2. A typical XRD patterns of the present sample, together with that for synthetic brochantite $Cu_4(OH)_6SO_4$ prepared by titrating a 0.1 M $CuSO_4$ solution with a 0.1 M NaOH solution until pH 10 [13].

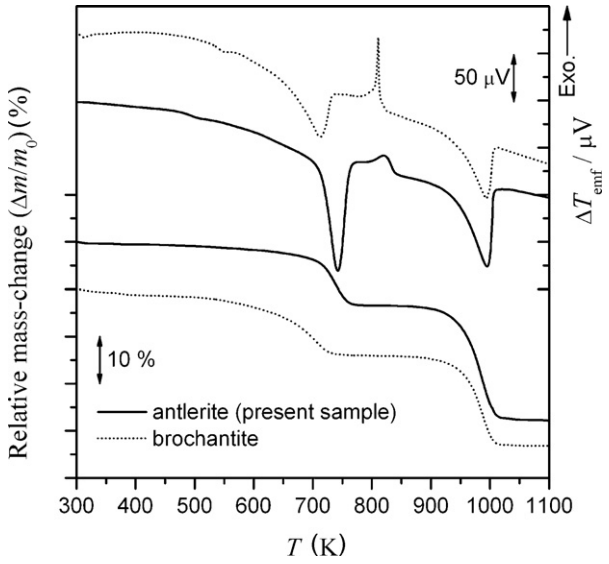

Fig. 4. Typical TG–DTA curves for the present sample and for $Cu_4(OH)_6SO_4$.

is known [7] that three well-distinct absorption peaks ascribed to O–H stretching vibration, i.e. 3587, 3389 and 3271 cm^{-1} in Fig. 3(b), are characteristic for $Cu_4(OH)_6SO_4$, due to three different OH groups having different degrees of hydrogen-bonding in the crystal. The present sample corresponding to $Cu_3(OH)_4SO_4$ indicated two separated absorption peaks in 3573 and 3485 cm^{-1}, which have been explained as the stretching vibrations of "free" OH and medium strength hydrogen-bridged OH, respectively [7].

Fig. 4 shows typical TG–DTA curves for the present sample, together with those for $Cu_4(OH)_6SO_4$. As has been reported [5–7,9], the thermal decomposition of $Cu_3(OH)_4SO_4$ proceeds in two separated mass-loss steps. The measured mass-loss values of the respective steps were $10.3 \pm 0.1\%$ and $22.0 \pm 0.1\%$, which are in agreement with the values of 10.2% and 22.6% calculated by assuming the following reactions:

$$Cu_3(OH)_4SO_4 \rightarrow Cu_3O_2SO_4 + 2H_2O \quad (1)$$

$$Cu_3O_2SO_4 \rightarrow 3CuO + SO_3 \quad (2)$$

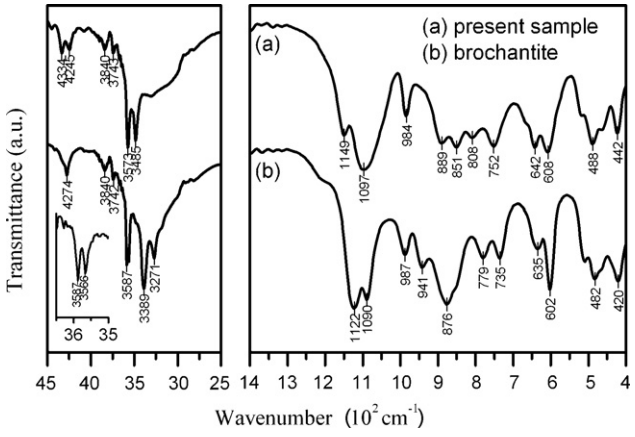

Fig. 3. Typical IR spectra for the present sample and for $Cu_4(OH)_6SO_4$.

All the above findings support the successful synthesis of antlerite $Cu_3(OH)_4SO_4$ by the microwave-assisted hydrothermal method by irradiating microwave for 1 min.

3.2. Thermal decomposition processes

By comparing the TG–DTA curves for $Cu_3(OH)_4SO_4$ and $Cu_4(OH)_6SO_4$ shown in Fig. 4, two contrasting features can be observed in addition to the differences in the mass-loss values of the respective reaction steps. One is the temperature range of the first mass-loss step which corresponds to dehydoxylation reaction. The dehydroxylation of $Cu_3(OH)_4SO_4$ initiates at a temperature higher by ca. 100 K than that of $Cu_4(OH)_6SO_4$. It is known that the dehydroxylation of $Cu_4(OH)_6SO_4$ proceeds via the following two separated reaction processes overlapped partially [1,15]:

$$Cu_4(OH)_6SO_4 \rightarrow Cu_4O(OH)_4SO_4 + H_2O \quad (3)$$

$$Cu_4O(OH)_4SO_4 \rightarrow Cu_4O_3SO_4 + 2H_2O \quad (4)$$

In comparison with $Cu_4(OH)_6SO_4$, the dehydroxylation of $Cu_3(OH)_4SO_4$ takes place in the similar temperature range with the second dehydroxylation step of $Cu_4(OH)_6SO_4$, i.e. Eq. (4).

The shapes of DTA exothermic peaks observed for the intermediate products in the temperature range of 750–850 K also indicate a large difference between the samples. It has been reported [1] that the sharp exothermic peak observed for the dehydration product of $Cu_4(OH)_6SO_4$ corresponds to the crystallization of dolerophanite Cu_2OSO_4 and tenorite CuO, where the enthalpy change for the crystallization processes varies depending on the controlled rate of dehydration reactions. Although an exothermic peak is also observed for $Cu_3(OH)_4SO_4$ in the similar temperature range, the shape of peak is broad and the peak area per unit mass of intermediate compound is smaller than that observed for $Cu_4(OH)_6SO_4$. As for the second mass-loss step corresponds to thermal desulfation, temperature

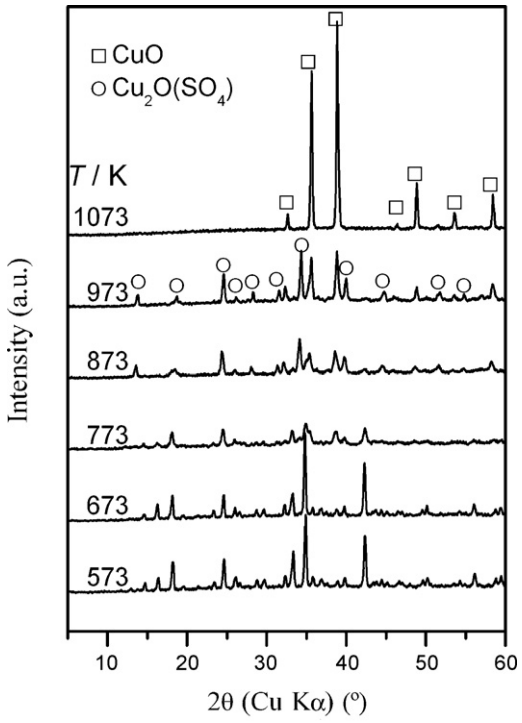

Fig. 5. Changes of the XRD patterns of the sample depending on the annealing temperature.

ranges and shapes of TG–DTA curves are very close between the samples.

Fig. 5 shows XRD patterns of the sample, $Cu_3(OH)_4SO_4$, annealed in air at various temperatures for 30 min. Change of the XRD patterns from 673 to 773 K indicates attenuations of the diffraction peaks ascribed to antlerite, but no new crystalline phase is observed. At 873 K, crystalline phases of dolerophanite Cu_2OSO_4 [16,17] and tenorite CuO [18] appear and grow further at 973 K. At 1073 K, only the crystalline phase of CuO is observed, indicating the formation of CuO by the decomposition of Cu_2OSO_4.

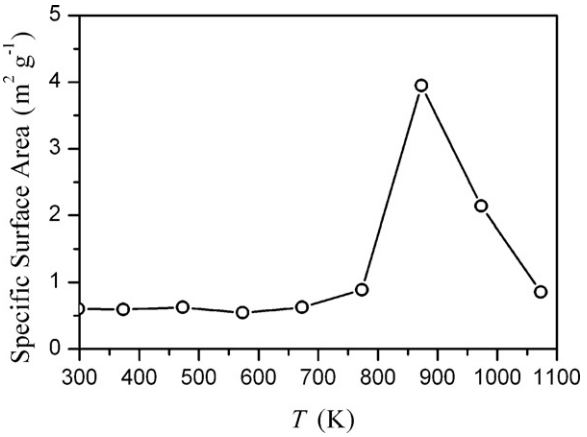

Fig. 6. Changes of the specific surface area of the sample depending on the annealing temperature.

Fig. 6 shows the change in specific surface area of the sample depending on the annealing temperature. The specific surface area remains constant up to 773 K and increases rapidly at 873 K with the partial crystallization of Cu_2OSO_4 and CuO during the dehydroxylation reaction. At the higher temperatures, the specific surface area decreases by the crystal growth of the intermediate compounds and the formation of final product CuO by the decomposition of Cu_2OSO_4. Fig. 7 shows typical SEM images of the samples annealed at 873 and 1073 K. The sample heated at 873 K remains the external form of the original crystallites, but pores are observed on the surface of the particles. Considering the rapid increase in the specific surface area at this temperature, it is probable that the sample particles become mere shells of the original crystallites at the reaction stage. The SEM image of the sample heated at 1073 K indicates the sintered aggregates of CuO particles. Deducing from the decrease in the specific surface area during the decomposition process of Cu_2OSO_4, it is expected that sintering of CuO particles is proceeding simultaneously with the decomposition reaction.

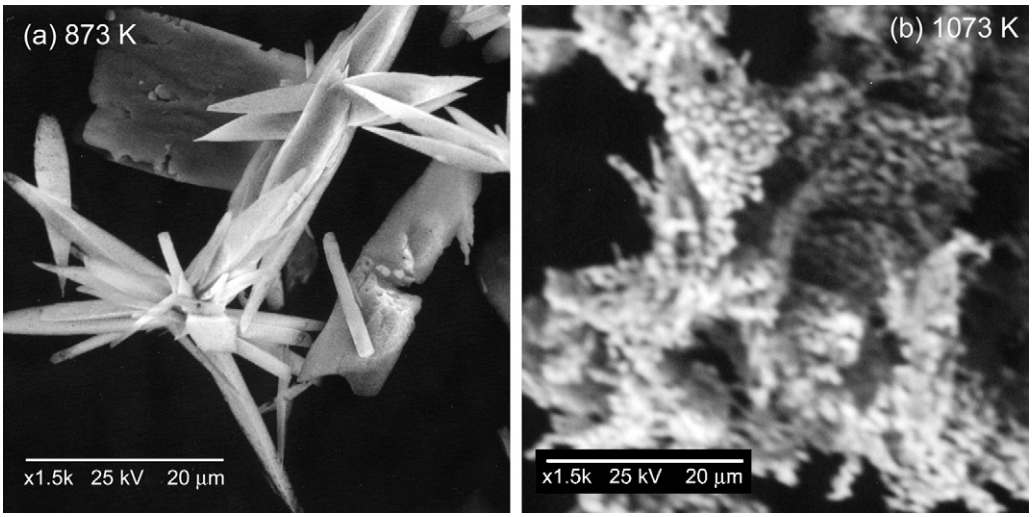

Fig. 7. Typical SEM images of the samples annealed at (a) 873 K and (b) 1073 K.

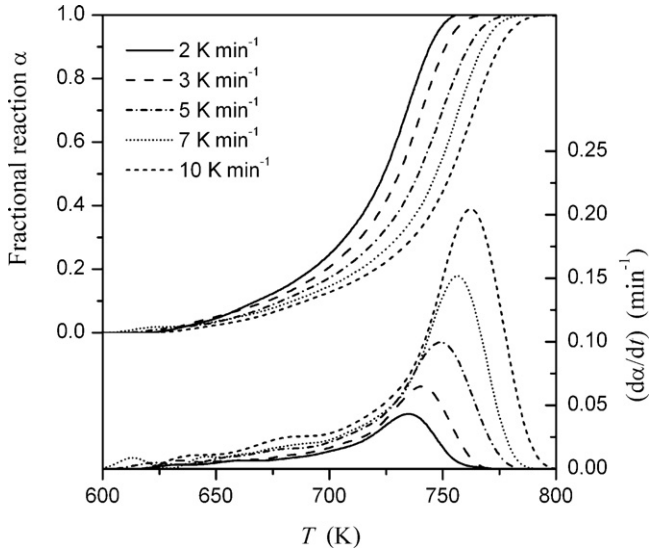

Fig. 8. The kinetic rate data at various heating rates for the dehydroxylation reaction of $Cu_3(OH)_4SO_4$.

3.3. Kinetics of dehydroxylation process

Fig. 8 shows the kinetic rate data at various heating rates for the dehydroxylation of $Cu_3(OH)_4SO_4$. Induction period-like behavior in the wide temperature range of ca. 100 K after initiating the dehydration reaction is characteristic of the kinetic rate data. The apparent activation energies, E_a, at various fractional reactions, α, were determined by Friedman method [19] according to the following equation:

$$\ln \frac{d\alpha}{dt} = \ln[Af(\alpha)] - \frac{E_a}{RT} \quad (5)$$

where A and $f(\alpha)$ are the pre-exponential factor and kinetic model function, respectively. The values of E_a calculated from the slopes of $\ln(d\alpha/dt)$ vs. T^{-1} plots at various constant α are shown in Fig. 9. After fluctuations of the E_a values at the very beginning of the reaction $\alpha < 0.1$, two distinguished α ranges with different constant values of E_a are observed in $0.1 \le \alpha \le 0.3$ and $0.4 \le \alpha \le 0.9$ with the averaged E_a values of 212.8 ± 7.2 and

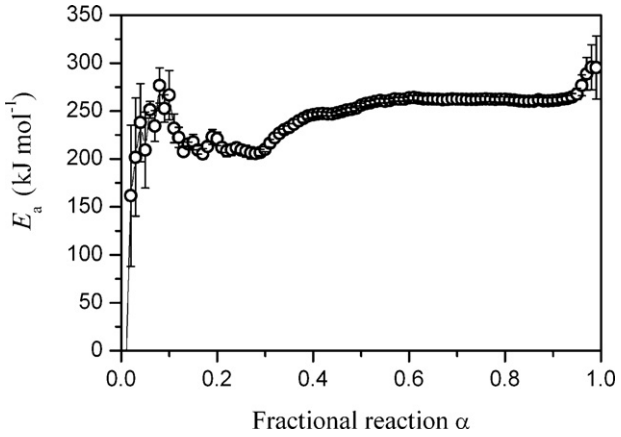

Fig. 9. The values of E_a at various constant α for the dehydroxylation reaction of $Cu_3(OH)_4SO_4$.

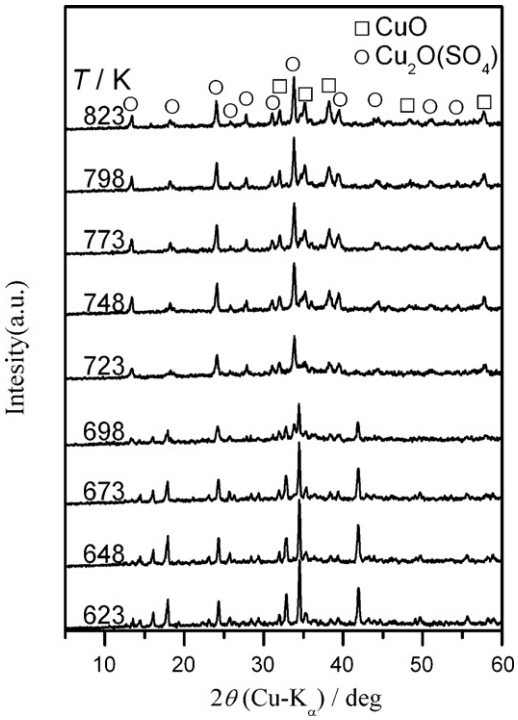

Fig. 10. Changes of XRD pattern of the sample during the course of dehydroxylation reaction.

$259.0 \pm 5.4\ kJ\ mol^{-1}$, respectively. The respective ranges of α with different constant E_a are apparently corresponding to the initial part of the reaction characterized by the induction period-like behavior and the established part of the reaction. As shown in Fig. 10, changes of XRD pattern of the sample during the course of reaction were recorded by heating stepwise the sample in steps of 25 K under flowing N_2 ($100\ cm^3\ min^{-1}$) for further detailed characterization of the initial and established parts of the dehydroxylation reaction. It is clearly seen that in the temperature range of initial part of reaction only the attenuations of the diffraction peaks due to $Cu_3(OH)_4SO_4$ are observed without indicating any new crystalline phase, whereas the crystalline phases of Cu_2OSO_4 and CuO appear in the temperature range of the established part of the reaction. Accordingly, the different values of E_a for the initial and established parts of the dehydration reaction can be interpreted as resulting from the change in the physico-geometric reaction mechanism.

By extrapolating the measured rate data to infinite temperature using the isoconversional relationships of Friedman plots at respective α, isothermal rate data of the initial and established parts of dehydration reaction were reproduced at infinite temperature. The reaction rate at infinite temperature at a selected α, $d\alpha/d\theta$, was calculated by the following equation using the measured rate data ($d\alpha/dt$, T) and experimental value of E_a [20,21]:

$$\frac{d\alpha}{d\theta} = \frac{d\alpha}{dt} \exp\left(\frac{E_a}{RT}\right) \quad (6)$$

where θ is the Ozawa's generalized time [22–24]. Fig. 11 shows the plots of $d\alpha/d\theta$ against α for the initial and established parts of the dehydroxylation reaction, where error bars indicate the

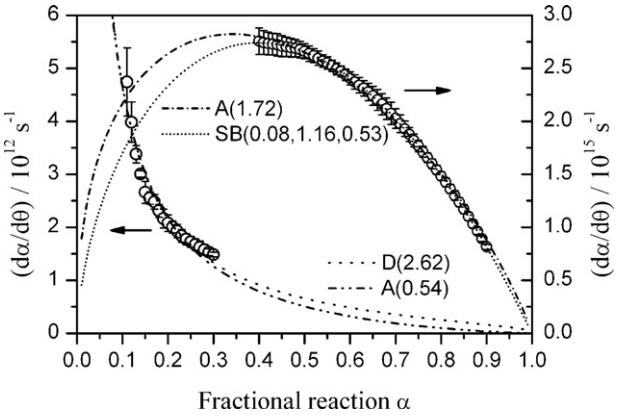

Fig. 11. The plots of $d\alpha/d\theta$ against α for the initial and established parts of the dehydroxylation reaction.

standard deviations of the $d\alpha/d\theta$ values calculated from the experimental data at different heating rates. The reaction rate and its changing behavior simulated at infinite temperature are largely different between the respective parts of the reaction.

The isothermal rate data at infinite temperature, $d\alpha/d\theta$ vs. α, recognized as the experimental master curve are related to the kinetic model function $f(\alpha)$ by the equation [20,21]:

$$\frac{d\alpha}{d\theta} = Af(\alpha) \quad (7)$$

Table 2 lists various $f(\alpha)$ assumed in the present study for evaluating the fitting to the experimental master curves, i.e. three different types of physico-geometric $f(\alpha)$ with non-integral kinetic exponents [15,25–29] and an empirical $f(\alpha)$ with three kinetic exponents known as Sestak–Berggren model [30]. On the basis of Eq. (7), the best values of the kinetic exponents of a selected $f(\alpha)$ and the value of pre-exponential factor A were determined simultaneously though the nonlinear least square fitting by the Levenberg–Marquardt optimization algorithm [31].

As shown in Fig. 11, the initial part of the reaction, $0.1 \leq \alpha \leq 0.3$, was fairly good fitted by the diffusion-controlled model D(n) with $n = 2.62$ and by the nucleation and growth model A(m) with $m = 0.54$, which are interpreted physico-geometrically as the contracting of reaction interface controlled by diffusion and formation of possible reaction sites controlled by diffusion of chemical species, respectively. Because the solid product of the dehydration reaction in the initial part is amorphous in view of XRD, both the physico-geometric mechanisms are probable at this stage of kinetic understanding.

As for the established part of the reaction $0.4 \leq \alpha \leq 0.9$, A(m) with $m = 1.72$ gave the best fitting to the experimental master curve within the physico-geomeric $f(\alpha)$ listed in Table 2. Although several interpretations based on the respective kinetics of nucleation and growth processes are possible for A(1.72), one of such nucleation and growth mechanisms is estimated as the most probable reaction mechanism of the established part of the dehydration reaction by considering the formations of crystalline Cu_2OSO_4 and CuO and the change in the morphology of the sample crystallites to be mere shells at this reaction stage. By applying an empirical SB(m,n,p) function, the experimental master curve of the established part of the reaction is nearly perfectly fitted by SB(0.08,1.16,0.53), which is due to really empirical characteristics of the function for fitting various physico-geometric types of reaction and those deviated cases as was recently demonstrated using SB(m,n) function with two kinetic exponents [32]. Because the physico-geometric A(1.73) can be correlated to the empirical SB(0,1,0.42), the validity of A(1.73) is also supported by the good correspondences of the respective three parameters between SB(0.08,1.16,0.53) and SB(0,1,0.42) from a view point of curve fitting.

Table 3 summarizes the kinetic results for the thermal dehydroxylation of $Cu_3(OH)_4SO_4$. By reviewing the kinetic behavior of the thermal dehydroxylation of $Cu_4(OH)_6SO_4$ reported previously [1], it was found that the second step of dehydroxylation expressed by Eq. (4) was described kinetically by D(2.6) or A(0.6) with the constant E_a value of 193 kJ mol^{-1} during the course of reaction $0.1 \leq \alpha \leq 0.9$, where the dehydration product, $Cu_4O_3SO_4$, was amorphous in view of XRD. The reported kinetic behavior for Eq. (4) and formation of the amorphous product are in good agreement with the present results for the initial part of the dehydration of $Cu_3(OH)_4SO_4$. The second step reaction of thermal dehydroxylation of $Cu_4(OH)_6SO_4$, i.e. Eq. (4), is regulated by such kinetics and mechanism during the whole course of reaction, whereas in the thermal dehyroxylation of $Cu_3(OH)_4SO_4$ the kinetic behavior changes to the nucleation and growth type on the way of the reaction. As the result, the dehydration product of $Cu_3(OH)_6SO_4$ is the mixture of the amorphous phase produced in the initial part and the crystalline phases of Cu_2OSO_4 and CuO produced in the established part of the dehydroxylation reaction. The differences in the shape and peak area of the DTA exothermic peaks observed for the dehydration products of $Cu_4(OH)_6SO_4$ and $Cu_3(OH)_4SO_4$, see Fig. 4, can be explained by the differences in the contents of amorphous phase in the respective dehydration products.

Table 2
Kinetic model functions $f(\alpha)$ employed in the present study

Model	Symbol	Range of exponent	$f(\alpha)$
Phase boundary controlled	R(n)	$1 \leq n \leq 3$	$n(1-\alpha)^{1-1/n}$
Diffusion controlled	D(n)	$1 \leq n < 2$	$[1-(1-\alpha)^{2/n-1}]^{-1}$
		$n = 2$	$[-\ln(1-\alpha)]^{-1}$
		$2 < n \leq 3$	$[(1-\alpha)^{2/n-1}-1]^{-1}$
Nucleation and growth	A(m)	$0.5 \leq n \leq 4$	$m(1-\alpha)[-\ln(1-\alpha)]^{1-1/m}$
Empirical	SB(m,n,p)	–	$\alpha^m(1-\alpha)^n[-\ln(1-\alpha)]^p$

Table 3
Kinetic results for the thermal decomposition of $Cu_3(OH)_4SO_4$

Reaction step	Range of α	E_a (kJ mol^{-1})	$f(\alpha)$	Kinetic exponents	A(s^{-1})	γ^{2a}
Dehydroxylation	$0.1 \le \alpha \le 0.3$	212.8 ± 7.1	D(n)	$n = 2.62 \pm 1.92$	$(1.17 \pm 2.77) \times 10^{11}$	0.9518
			A(m)	$m = 0.54 \pm 0.02$	$(1.38 \pm 0.11) \times 10^{12}$	0.9425
	$0.4 \le \alpha \le 0.9$	259.0 ± 5.4	A(m)	$m = 1.72 \pm 0.02$	$(3.59 \pm 0.03) \times 10^{15}$	0.9975
			SB(m,n,p)	$m = 0.08 \pm 0.22$ $n = 1.16 \pm 0.07$ $p = 0.53 \pm 0.20$	$(7.60 \pm 0.23) \times 10^{15}$	0.9999
Desulfation	$0.1 \le \alpha \le 0.9$	240.7 ± 13.5	R(n)[b]	$n = 1.00$	$(2.85 \pm 0.01) \times 10^{10}$	–
			SB(m,n,p)	$m = -2.51 \pm 0.10$ $n = 1.29 \pm 0.04$ $p = 2.58 \pm 0.09$	$(3.17 \pm 0.03) \times 10^{10}$	0.9979

[a] Correlation coefficient of the nonlinear regression analysis.
[b] Within restricted range $0.2 \le \alpha \le 0.6$.

We acknowledge that some more detailed experiments of clarifying the texture/crystallographic relations between the reactant and product solids are required for interpreting the actual physico-chemical meanings of the respective kinetic model functions evaluated by the present curve fitting method. At the same time, large influences of the atmospheric water vapor on the overall kinetics of the dehydroxylation process and on the crystallinity/texture of the solid products at this stage have been confirmed by our preliminary experiments. By grasping such apparent kinetic behaviors as one of the special characteristics of the thermal decomposition of solids, it is expected that coming systematic examinations for the interactions of the atmospheric water vapor with the reactant and product solids and these influences on the kinetics of the dehydroxylation process will contribute notably towards the provision of a theoretical foundation for the physico-geometric approaches to the kinetics of the solid-state reactions.

3.4. Kinetics of desulfation process

Fig. 12 shows the kinetic rate data at various heating rates for the desulfation reaction of Cu_2OSO_4. The overlapping of all the differential rate data, $d\alpha/dt$ vs. T, at different heating rates in the acceleration part is characteristic of the kinetic rate data. The values of E_a calculated from the slope of Friedman plots at various α were shown in Fig. 13. Although a trend of slight decrease in the values of E_a depending on α is observed, the value averaged over $0.1 \le \alpha \le 0.9$ was 240.7 ± 13.5 kJ mol^{-1}, which is in good agreement with the reported values for the isothermal and nonisothermal desulfation of Cu_2OSO_4 during the course of the thermal decomposition of $Cu_4(OH)_6SO_4$, i.e. 259.1 and 252.6 kJ mol^{-1}, respectively [1].

Fig. 14 shows the plots of $d\alpha/d\theta$ against α calculated using the averaged value of $E_a = 240.7 \pm 13.5$ kJ mol^{-1}, where error bars indicate the standard deviations of the $d\alpha/d\theta$ values calculated from the experimental data at different heating rates. The reaction proceeds at the constant rate until α reaches around 0.6, which is interpreted as the zero-order rate behavior expressed by R(n) with $n = 1$, i.e. $f(\alpha) = 1$. For the solid-state reaction, one-dimensional advancement of reaction interface controlled by chemical events is one of the typical cases of the zero-order rate behavior. As for the present reaction, such reaction mechanism is understood probably as the advancement of the overall reaction interface from the top surface of the assemblage of sample particles in the sample pan to the bottom, which is supported by the fact that the reactant in this reaction step is a pellet-like aggregate which has been formed by the volume shrinkage of sample assemblage through the previous dehydroxylation reaction and in situ crystallization of the dehydration products.

In the later part of the reaction $\alpha > 0.6$, the reaction rate decelerates gradually as reaction advances. Practically the same rate behavior has been reported for the thermal desulfation of Cu_2OSO_4 during the course of isothermal and nonisothermal decomposition of $Cu_4(OH)_6SO_4$ [1]. The situation of the reacting sample at this stage is deduced as follows. Originally, the reactant solid of the present desulfation reaction is a mixture of CuO and Cu_2OSO_4 in the molar ratio of $CuO/Cu_2OSO_4 = 1$.

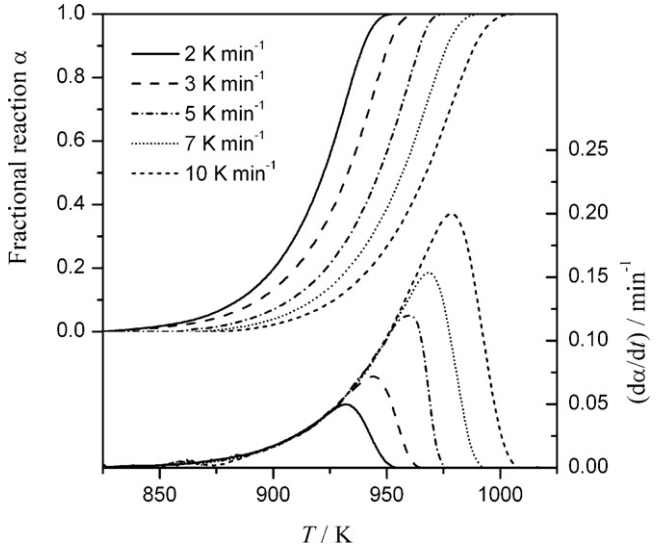

Fig. 12. The kinetic rate data at various heating rates for the desulfation reaction of Cu_2OSO_4.

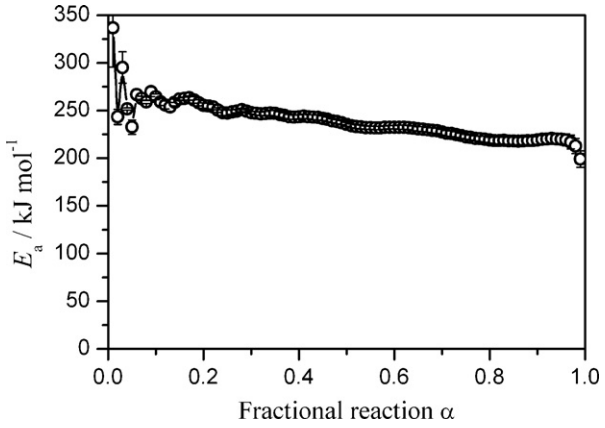

Fig. 13. The values of E_a at various constant α for the desulfation reaction of Cu_2OSO_4.

By the thermal desulfation reaction, aggregated layer of CuO is produced as the solid product layer, where the sintering of CuO particles takes place concurrently with the reaction as was observed in Fig. 7(b). As a result, the gross diffusion of the evolved SO_3 ($\rightarrow SO_2 + (1/2)O_2$) produced at the reaction interface through the solid product layer becomes difficult gradually as reaction advances and the partial pressure at the reaction interface increases.

In the most simple case, such rate behavior is interpreted by the α-dependent change in the reaction geometry at the later part of the reaction without changing the kinetics of the interface reaction, which is assumably from one-dimensional advancement of a flat reaction interface assumed for R(1.00) to two-dimensional shrinkage of semi-spherical reaction interface due to the difficulty of the diffusional removal of the evolved gas through the solid product layer produced at the first-half reaction. By the nonlinear least square fitting based on Eq. (7), SB(−2.51,1.29,2.58) was determined as the empirical function to give the best fit to the experimental master curve in the range $0.1 \leq \alpha \leq 0.9$, see Fig. 14 and Table 3. In this case, SB(−2.51,1.29,2.58) is interpreted as an empirical accommodation function $a(\alpha)$ to accommodate the α-dependent deviation of the actual reaction geometry from the ideal $f(\alpha)$ = R(1.00) and

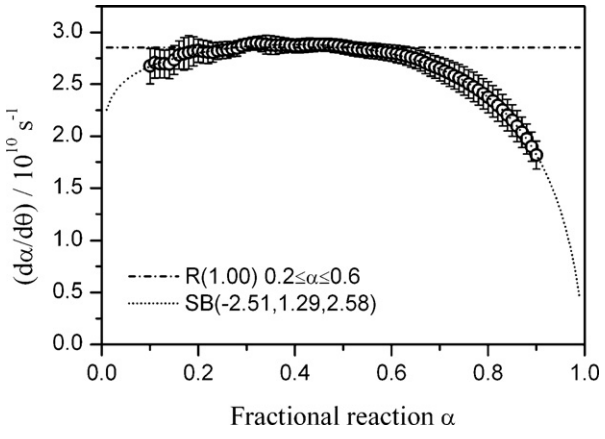

Fig. 14. The plots of $d\alpha/d\theta$ against α for the desulfation reaction of Cu_2OSO_4.

the following equation can be formalized [33,34]:

$$\frac{d\alpha}{dt} = A \exp\left(-\frac{E_a}{RT}\right) f(\alpha) a(\alpha) \quad (8)$$

It is also worth noting that, if the overall reaction is described satisfactorily by Eq. (8) irrespective of the heating rate applied, the apparent values of E_a determined by an isoconversional method should indicate the constant value during the course of reaction [29,35]. As for the present reaction under linearly increasing temperature, however, a trend of slight but systematic decrease in the apparent values of E_a with α is observed as shown in Fig. 13. For such changes of E_a depending on α, several possible reasons are presumed. Because the degree of sintering changes with temperature, it is probable that the appropriate $a(\alpha)$ changes depending on the heating rate applied. The partial pressure of the evolved gas, P, at the reaction interface also changes with α and heating rate applied. Influence of P on the reaction rate is formalized in some cases as [36,37]:

$$\frac{d\alpha}{dt} = A \exp\left(-\frac{E_a}{RT}\right) f(\alpha) \left(1 - \frac{P}{P_0}\right) \quad (9)$$

where P_0 is the equilibrium pressure. At a selected α, if the accommodation functions such as $a(\alpha)$ in Eq. (8) and $\alpha(P,T) = (1 - P/P_0)$ in Eq. (9) are not maintained constant among different heating rates, errors are introduced into the value of E_a calculated from the slope of the Friedman plot, i.e. Eq. (5) [29,34,38]. The systematic change in the error depending on α is one of the possible reasons for the α-dependent variation of E_a. In the more complicated case, the α-dependent E_a is assumed for the overall reaction regulated by a combined effects of more than one kinetic processes with different activation energies, where the contributions of the respective kinetic processes change depending on α and heating rate applied [39,40]. In the present reaction, these interdependent kinetic processes may be chemical reaction at the reaction interface, diffusion of evolved gas through the solid product layer and sintering of CuO in the solid product layer.

Further detailed kinetic evaluation for the present desulfation reaction is highly desired as a model reaction for the thermal decomposition of a solid accompanied by the sintering of solid product, because such type of reaction processes is common in the processing of ceramic materials through the thermal decomposition route and influences largely on the properties of the produced ceramic materials. Systematic kinetic study for the thermal decomposition of Cu_2OSO_4 mixed with CuO in different molar ratios under various reaction conditions will be reported separately for discussing the problems remaining unsolved in the present study.

4. Conclusion

(1) Needle-like crystals of synthetic antlerite $Cu_3(OH)_4SO_4$ (ca. 20–30 μm in length) is prepared by the microwave-assisted hydrothermal method from a mixed solution of $CuSO_4$ and urea by irradiating microwave for 1 min.
(2) The thermal decomposition of $Cu_3(OH)_4SO_4$ proceeds via well distinguished two-reaction steps of dehydroxylation

and desulfation to produce CuO, where crystalline phases of Cu_2OSO_4 and CuO appear as the intermediate products by the dehydroxylation reaction.

(3) The nonisothermal dehydroxylation of $Cu_3(OH)_4SO_4$ is characterized kinetically by two different parts of reaction mechanism. The initial part of the reaction is controlled by diffusion with $E_a = 212.8 \pm 7.2\,kJ\,mol^{-1}$, where an amorphous product is produced. The reaction mechanism changes to a nucleation and growth-type with $E_a = 259.0 \pm 5.4\,kJ\,mol^{-1}$ on the way of the reaction. In the established part of the reaction, crystalline phases of Cu_2OSO_4 and CuO are produced. After completing the mass-loss due to dehydration, amorphous intermediate phase produced during the initial part of reaction is crystallized to Cu_2OSO_4 and CuO in the temperature range of 750–850 K.

(4) As for the desulfation process, one-dimensional advancement of the overall reaction interface in an aggregate of reactant particles was predominant with $E_a = 240.7 \pm 13.5\,kJ\,mol^{-1}$, but the process was influenced largely by the sintering of CuO in the solid product layer especially in the later part of the reaction.

Acknowledgement

The present work is supported partially by a grant-in-aid for scientific research (B) (No. 18300267) from Japan Society for the Promotion of Science.

References

[1] N. Koga, J.M. Criado, H. Tanaka, J. Therm. Anal. 49 (1997) 1467.
[2] N. Koga, J.M. Criado, H. Tanaka, Thermochim. Acta 340/341 (1999) 387.
[3] N. Koga, J.M. Criado, H. Tanaka, J. Therm. Anal. Cal. 60 (2000) 943.
[4] N. Koga, S. Yamada, Int. J. Chem. Kinet. 37 (2005) 346.
[5] G. Pannetier, J.M. Bregeault, G. Djega-Mariadassou, M. Grandon, Bull. Soc. Chim. France (1963) 2616.
[6] P. Ramamurthy, E.A. Secco, Can. J. Chem. 48 (1970) 3510.
[7] E.A. Secco, Can. J. Chem. 66 (1988) 329.
[8] F.C. Hawthorne, L.A. Groat, R.K. Eby, Can. Mineral. 27 (1989) 205.
[9] I.V. Lin'ko, A.B. Kukikov, N.U. Venskovshi, N.N. Lobanov, O.V. Rudnitskatya, Z. Neorg. Khim. 46 (2001) 1622.
[10] S. Vilminot, M. Richard-Plouet, G. Andre, D. Swierczynski, F. Bouree-Vigneron, E. Marino, M. Guillot, Cryst. Eng. 5 (2002) 177.
[11] S. Vilminot, M. Richard-Plouet, G. Andre, D. Swierczynski, M. Guillot, F. Bouree-Vigneron, M. Drillon, J. Solid State Chem. 170 (2003) 255.
[12] H.M. Kingston, S.J. Haswell (Eds.), Microwave-Enhanced Chemistry, American Chemical Society, Washington, DC, 1997.
[13] H. Tanaka, N. Koga, J. Chem. Educ. 67 (1990) 612.
[14] JCPDS 7-0407.
[15] N. Koga, J. Malek, Thermochim. Acta 282/283 (1996) 69.
[16] H. Effenberger, Monatsh. Chem. 116 (1985) 927.
[17] JCPDS 46-0005.
[18] JCPDS 44-0706.
[19] H.L. Friedman, J. Polym. Sci. C 6 (1964) 183.
[20] T. Ozawa, J. Therm. Anal. 31 (1986) 547.
[21] N. Koga, Thermochim. Acta 258 (1995) 145.
[22] T. Ozawa, Bull. Chem. Soc. Jpn. 38 (1965) 1881.
[23] T. Ozawa, J. Therm. Anal. 2 (1970) 301.
[24] T. Ozawa, Thermochim. Acta 100 (1986) 109.
[25] J. Sestak, J. Therm. Anal. 33 (1988) 1263.
[26] N. Koga, J. Malek, J. Sestak, H. Tanaka, Netsu Sokutei 20 (1993) 210.
[27] R. Ozao, M. Ochiai, J. Ceram. Soc. Jpn. 101 (1993) 263.
[28] N. Koga, H. Tanaka, J. Therm. Anal. 41 (1994) 455.
[29] N. Koga, H. Tanaka, Thermochim. Acta 388 (2002) 41.
[30] J. Sestak, G. Berggren, Thermochim. Acta 3 (1971) 1.
[31] D.M. Bates, D.G. Watts, Nonlinear Regression and its Applications, Wiley, New York, 1988.
[32] L.A. Perez-Maqueda, J.M. Criado, P.E. Sanchez-Jimenez, J. Phys. Chem. A 110 (2006) 12456.
[33] J. Sestak, J. Therm. Anal. 36 (1990) 1977.
[34] N. Koga, J. Therm. Anal. 49 (1997) 45.
[35] N. Koga, J.M. Criado, J. Am. Ceram. Soc. 81 (1998) 2901.
[36] M. Reading, D. Dollimore, R. Whitehead, J. Therm. Anal. 37 (1991) 2165.
[37] J.M. Criado, M. Gonzalez, J. Malek, A. Ortega, Thermochim. Acta 254 (1995) 121.
[38] N. Koga, J. Sestak, J. Am. Ceram. Soc. 83 (2000) 1753.
[39] S. Vyazovkin, N. Sbirrazzuoli, Macromolecules 29 (1996) 1867.
[40] S. Vyazovkin, N. Sbirrazzuoli, Macromol. Rapid Commun. 27 (2006) 1515.